Effect of microstructure on load-carrying and energy-dissipation capacities of UHPC

Jonathan J. Buck, David L. McDowell, Min Zhou *

The George W. Woodruff School of Mechanical Engineering, The School of Materials Science and Engineering, Georgia Institute of Technology, Atlanta, GA 30332-0405, USA

ARTICLE INFO

ABSTRACT

The load-carrying and energy dissipation capacities of ultra-high performance concrete (UHPC) under dynamic loading are evaluated in relation to microstructure composition at strain rates on the order of 10^5 s^{-1} and pressures of up to 10 GPa. Analysis focuses on deformation and failure mechanisms at the mesostructural level. A cohesive finite element framework that allows explicit account of constituent phases, interfaces, and fracture is used. Three modes of energy dissipation are tracked, i.e., inelastic deformation, distributed cracking, and interfacial friction. Simulations are carried out over a range of volume fractions of constituent phases. Results show that (1) volume fractions of the constituents have more influence on the energy-dissipation than load-carrying capacity, (2) inelastic deformation is the source of over 70% of the energy dissipation, and (3) the presence of porosity changes the role of fibers in the dissipation process. Microstructure–behavior relations are established to facilitate materials design for target-specific applications.

1. Introduction

Ultra-high-performance concrete (UHPC) is a relatively new and advanced building material that provides several advantages over conventional concrete. Benefits include significantly enhanced ductility and energy-absorption capabilities [1–4] that lead to compressive strengths in excess of 150 MPa and flexural strengths of over 200 times those of conventional concrete [5]. These attributes are possible, because UHPC has several unique characteristics that set it apart from more conventional forms of concrete, including finer quartz aggregate, a lower water-to-cement ratio, and the presence of superplasticizers and fine ductile metal or polymer fibers. These properties lend UHPC to structural applications in which resistance to blast and impact is of paramount importance. Designing UHPC structures that are resilient to such extreme loading events requires that the material has high strength, the capacity to dissipate much of the imparted energy, and the capability to attenuate the stress caused by the loading. However, it is not clear how the characteristics of UHPC at the microstructural level determine these attributes. In particular, the effects of the constituent volume fractions on load-carrying and energy-dissipation capacities under high-rate loading have not been systematically quantified using realistic micromechanical models. Establishing these relationships is important, as the relations can be used to tailor UHPC structures to mitigate specific threats.

The large number of design variables at the microstructural level, such as volume fractions of constituent phases, microstructure morphology, constituent size scales, constituent behaviors, and interfacial bonding strength, pose a challenge in exploring microstructure-property/

response relations. Developing comprehensive structure–property relations, however, requires that these variables and their interactions be analyzed. The influence of microstructure can be investigated using experimental methods and/or numerical techniques. The use of experimental methods is expensive and lengthy for such complex systems, because the number of experiments needed for such a task can quickly grow beyond allowable financial and time constraints. Experiments are limited to samples that are physically available and cannot be used to analyze materials that do not yet exist. Additionally, deformation processes involved in the dynamic response of UHPC, including distributed microcracking, friction, and granular flow, are inherently coupled phenomena that are difficult to fully capture separately using experimental methods. Nonetheless, these processes and their interactions must be quantified to tailor materials for specific applications.

Numerical simulations offer a useful means for establishing microstructure–performance relations. Much of the published literature involving numerical simulations of concrete implements homogenized phenomenological constitutive relations at the macrostructural scale. For example, Mroz and Angelillo developed a rate-dependent model for concrete [6]. The model makes use of a damage surface with an associated flow rule to account for stiffness degradation. Voyiadjis and Taqieddin developed an elasto-plastic damage model for concrete materials that uses the crack density to quantify the degradation in the elasticity tensor [7]. The model is capable of reproducing the post-failure softening behavior that is representative of concrete. A similar model was also developed by Fanella and Krajcinovic [8]. Grassl and Jirásek developed a damage-plasticity model that incorporates the effective stress to account for plasticity and the plastic strain to account for damage [9]. The model was applied on the structural scale to analyze a reinforced concrete column and successfully captured the qualitative nature of experimental load–displacement curves. A number of other hydrocode

* Corresponding author. Tel.: +1 404 894 3294.
E-mail address: min.zhou@gatech.edu (M. Zhou).

models are available for simulating the nonlinear dynamic responses of concrete structures [10].

Mesoscale simulations that fully account for the heterogeneous nature of concrete can help explain the micro-scale processes that give rise to the observed structural response on the macro-scale. Park, Xia, and Zhou [11] conducted numerical simulations at the mesoscale using a fully dynamic finite element model to systematically study the effect of aggregate volume fraction on the strength and energy dissipation capacity of plain concrete. Their micromechanical model explicitly accounts for the two-phase structure of cementitious matrix and quartz aggregate of plain concrete. The simulations concern strain rates on the order of 10^4 s^{-1} and hydrostatic pressures up to 1.5 GPa. The results show that an aggregate volume fraction of 42% leads to a 15% improvement in energy-dissipation capacity and a 30% enhancement in strength as compared to plain mortar. Aragao et al. [12] conducted simulations using a cohesive finite element model to analyze fracture and failure in concrete at the microstructural level in which the two-phase structure of cementitious matrix and quartz aggregate is explicitly modeled. Cohesive traction and fracture energy parameters are calibrated in a manner that allows the model to accurately represent experimental data from quasi-static tensile tests. Xu, Hao, and Li [13] performed a similar study involving a mesoscale numerical model of fiber-reinforced concrete that provide explicit account of the matrix, aggregate, and fiber phases. The study considered the effects of aggregate and fiber size distribution, as well as fiber volume fraction, on the dynamic compressive strength of fiber-reinforced concrete. The results show that fiber volume fractions in the range of 0.6% to 1.8% do not appreciably change the compressive dynamic inflation factor, i.e., at a given strain rate, dynamic compressive strength is independent of fiber content. Bolander and Lim [14] developed a lattice model with discrete representations of fibers and the interface between fibers and the cementitious matrix to assess the effects of fiber distribution on the durability mechanics of fiber-reinforced concrete.

Lammi et al. [15] investigated the dynamic fracture and dissipation behavior of concrete at several levels of hierarchy of microstructure/mesostructure using a cohesive finite element model that accounts for crack formation and frictional dissipation at crack faces. The nominal strain rate considered is on the order of 10^3 s^{-1}. Quartz aggregate and porosity are explicitly modeled, along with the interface between the phases. The volume fractions of quartz and porosity considered are in the ranges of 0–40% and 0–5%, respectively. The results show that the concrete with 40% aggregate by volume has a load-carrying capacity that is up to 12.2% higher than that of pure matrix without aggregate. A porosity level of 5% decreases the load-carrying capacity by up to 10.9%. Porosity is also found to have the most significant effect on energy dissipation by enhancing plastic deformation.

Ellis et al. [16] carried out numerical simulations of 3D microstructures with explicit resolution of porosity and steel fibers within a cementitious matrix. The interface between fibers and matrix was also explicitly modeled. At strain rates of 5×10^2–10^3 s^{-1}, increasing the fiber volume fraction from 0% to 2% is found to increase the load-carrying capacity by up to 19%. The energy dissipation is found to depend most significantly on the fiber volume fraction. In contrast,

porosity has only a minor influence on energy dissipation. The foregoing mesoscale simulations are summarized in Table 1.

A number of issues have yet to be addressed. First and foremost, there has not been a thorough and systematic characterization of the dynamic behavior of UHPC. In particular, the material performance in relation to the volume fractions of constituents has not been investigated over a sufficiently wide range. Numerical simulations are needed that consider the essential deformation mechanisms that occur at the microstructural level, including fracture, friction, and inelastic granular flow [17]. There is a lack of understanding on how these microstructural-level mechanisms affect macroscopic responses of the overall composites. Many of the analytical models developed in the open literature to characterize these relationships require an excessive number of material parameters, some of which have no basis in the physical processes underlying the material behavior [18]. Consequently, these models are often applicable only to relatively narrow ranges of compositions and loading conditions specific to the experiments on which the phenomenological constitutive relations are based [19]. Additionally, there have been no studies on the attenuation of stress waves as they traverse heterogeneous UHPC microstructures. There have also been no studies on the relative contributions of mechanisms for energy dissipation as a stress wave propagates through the structure, which has been identified by a panel of experts as a fundamental research need in the field of fiber-reinforced cement [20]. Also, the constituents in UHPC are known to undergo phase transformations under conditions with high temperatures and high pressures resulting from loading of sufficient magnitudes. In particular, at pressures above 2.35 GPa, the quartz aggregate phase in concrete undergoes a phase transformation from α-quartz to coesite, which involves a volume change of 8.82%. The effects of such phase transformations of constituents in UHPC on the overall mechanical response of the material have not been quantified. This paper focuses on the behavior without phase transformations. The effect of the pressure-induced α-quartz-to-coesite phase transformation of the quartz aggregate is analyzed in [21].

In the analysis conducted here, a micromechanical cohesive finite element model (CFEM) similar to that used by Lammi et al. [15] is adopted to allow explicit resolution of the constituents in the concrete microstructure, including the cementitious matrix, aggregate, fibers, and voids. The model also allows explicit account of crack formation and frictional interaction between crack surfaces that come into contact under compression. This approach enables the contributions of different dissipation mechanisms (bulk inelasticity, fracture/crack formation, and interfacial friction) to be tracked and quantified. Additionally, this approach captures the interaction and coupling of the dissipation processes at the microstructural level. The composition of the microstructure is systematically varied over a wide range to delineate the effects of each material constituent. Simulations are carried out at strain rates on the order of 10^4 s^{-1}. The analyses also focus on the correlation between volume fractions of constituent phases and macroscopic response in terms of load carried, stress attenuation, crack formation, and energy dissipated. The results are used to develop microstructure–performance relation maps that can be used to identify desired material design parameters for specific application conditions.

Table 1
Summary of mesoscale numerical simulations of UHPC reported in the literature.

Researchers	$V_a(\%)$	$V_p(\%)$	$V_f(\%)$	$\dot{\varepsilon}(s^{-1})$	Interfaces (yes/no)?
Park, Xia, and Zhou	[0, 10, 15, 22, 32, 42]	–	–	10^4	N
Aragao, et al.	N/A[1]	–	–	0.01	Y
Xu, Hao, and Li	40%	–	[0.6, 1.2, 1.8]	0.45–427	N
Bolander and Lim	N/A[1]	–	N/A[a]	N/A[1]	Y
Lammi, McDowell, and Zhou	[10, 20, 30, 40]	[0, 2.5, 5]	–	5×10^3	Y
Ellis, McDowell, and Zhou	–	[1,5,10]	[0, 2, 4]	5×10^3	Y

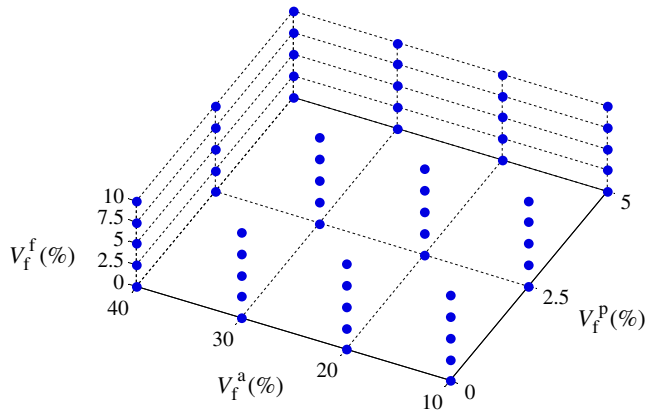[a] N/A indicates that the value was not explicitly stated in the work.

Fig. 1. Microstructure design space with combinations of constituent volume fractions analyzed.

Table 2
Diameters of quartz, porosity, and fibers used for all microstructures in the numerical simulations.

Phase	Diameter (μm)
Quartz	600
Porosity	100
Fiber	200

2. Microstructure instantiation

One of the goals of this work is to thoroughly characterize the dynamic behavior of UHPC over a wide range of constituent volume fractions. This necessitates a large number of microstructural instantiations. A total of 60 unique microstructures are generated with idealized 2D morphologies, reflecting all combinations of the aggregate, void, and fiber contents. The parametric range of constituent volume fractions is shown in Fig. 1. Five sample microstructures are shown in Fig. 2 to illustrate the variation in the volume fractions of the constituents. The microstructures analyzed are generated in a manner similar to that in Lammi et al. [15]. The purpose of this study is to quantify the load-carrying and energy-dissipation capacities of UHPC as functions of the volume fractions of phases, rather than phase size or size distribution. The effect of morphology of the constituents is beyond the scope of the current work and is reserved for future study. Consequently, each of the phases has a fixed size with no deviation, as shown in Table 2. The fibers, idealized as ellipses in 2D, are given a constant ellipticity ratio of 5:1. The microstructure samples are 5 by 20 mm in size.

3. Constitutive relations

3.1. Cementitious matrix

Cementitious materials are both pressure-sensitive and rate-sensitive, so the constitutive relation used must be able to capture both aspects of the behavior. In this study, the Drucker–Prager model is used for the cementitious matrix [22]. The Drucker–Prager relation assumes the yield condition

$$F = t - p\tan(\beta) - d \leq 0, \tag{1}$$

where

$$t = \frac{1}{2}q\left[1 + \frac{1}{K} - \left(1 - \frac{1}{K}\right)\left(\frac{r}{q}\right)^3\right]. \tag{2}$$

In the above equations, p is the hydrostatic pressure, β is the internal friction angle in the meridional stress plane, d is the yield stress of the material under pure shear, q is the von Mises equivalent stress, given by $q = \sqrt{\frac{3}{2}\mathbf{S} : \mathbf{S}}$, K is the ratio between the yield stress in triaxial tension and the yield stress in triaxial compression, and r is the third invariant of the deviatoric stress, given by $r = \sqrt[3]{\frac{9}{2}\mathbf{S}\cdot\mathbf{S} : \mathbf{S}}$. In the preceding expressions, $\mathbf{S}$ is the deviatoric stress tensor. Parameter K allows for tension-compression asymmetry on any arbitrary π-plane. To ensure a convex yield surface, the value of K is restricted to the range $0.778 \leq K \leq 1.0$. Setting $K = 1$ removes the dependence on the third invariant of the deviatoric stress, and Eq. (1) reduces to the classical Drucker–
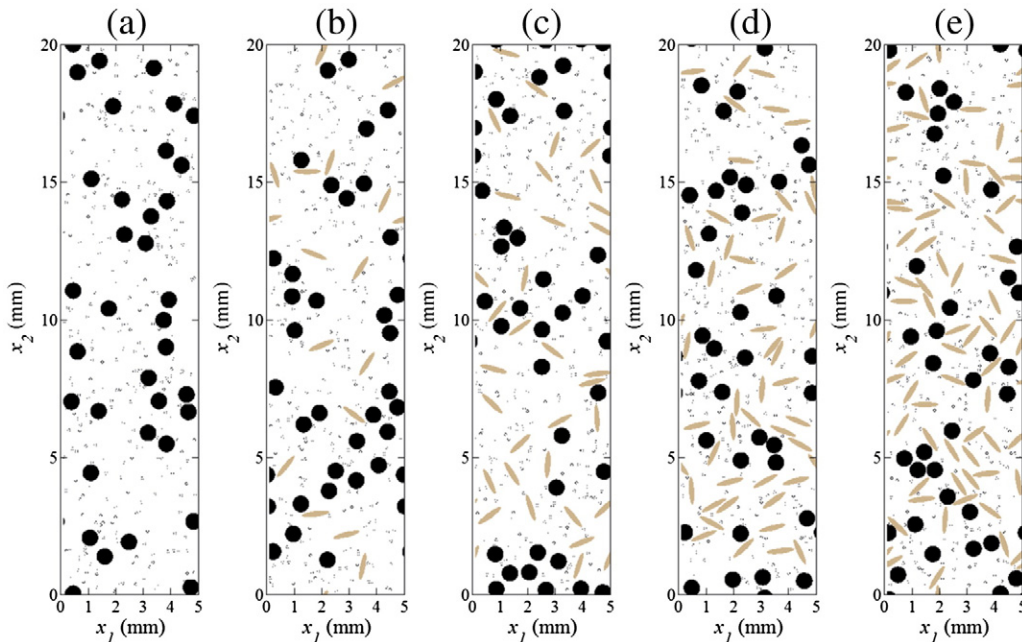

Fig. 2. Microstructures with 10% aggregate, 2.5% porosity, and (a) 0% fibers, (b) 2.5% fibers, (c) 5% fibers, (d) 7.5% fibers, and (e) 10% fibers.

Prager yield criterion [23]. Furthermore, when $K = 1$ and $\beta = 0$, Eq. (1) reduces to the von Mises yield criterion.

Because cementitious paste exhibits dilatation and is a non-associative material, the yield function F does not serve as the plastic flow potential. Instead, a scalar flow potential G is chosen such that

$$G = t - p \tan(\psi),\tag{3}$$

where ψ is the dilation angle. After yielding, a material with non-associated flow has the rate of plastic deformation tensor

$$D^{pl} = \frac{\dot{\bar{\varepsilon}}^{pl}}{c}\frac{\partial G}{\partial \sigma},\tag{4}$$

where $\dot{\bar{\varepsilon}}^{pl}$ is the equivalent plastic strain rate, defined by

$$\dot{\bar{\varepsilon}}^{pl} = \sqrt{\frac{2}{3}\mathbf{D}^{pl}:\mathbf{D}^{pl}},\tag{5}$$

and

$$c = 1 - \frac{1}{3}\tan\psi.\tag{6}$$

The values used for the Drucker–Prager constitutive relation in this study are provided in Table 3 [11].

3.2. Quartz aggregate

The quartz aggregate is given rate-independent linear elastic properties. The quartz aggregate is assigned an elastic modulus of 97 GPa and a Poisson's ratio of 0.08 [15]. The brittle nature of quartz suggests that it will fail in shear or tension. However, the presence of cohesive elements accounts for this mode of failure.

3.3. Steel fibers

The Johnson–Cook model is used to describe the behavior of the steel fibers. This model allows the rate-dependent hardening behavior of steel to be accounted for. The Johnson–Cook constitutive relation can be expressed as

$$\bar{\sigma}\left(\bar{\varepsilon}^p,,\dot{\varepsilon}^p,T\right) = \left(A + B\bar{\varepsilon}^n\right)\left[1 + C\log\left(\frac{\dot{\varepsilon}^p}{\dot{\varepsilon}_0}\right)\right]\left[1 - \left(\frac{T - T_{tr}}{T_m - T_{tr}}\right)^m\right].\tag{7}$$

Here, A, B, C, and m are material parameters that are calibrated using experimental data [24]. The first expression on the right hand side accounts for strain hardening, the second expression accounts for strain-rate hardening, and the third expression accounts for thermal softening. Model parameters are listed in Table 4. The introduction of reinforcing steel fibers also requires the appropriate calibration of cohesive bonding between the fibers and the cement matrix. The peak traction and fracture energy of the fiber-cement interface are in line with values obtained from experimental data for fiber-reinforced cement [25,26].

Table 3
Parameters used in Drucker–Prager constitutive relation.

Density (g/cm³)	2.4
Elastic modulus (GPa)	22.9
Poisson's ratio	0.2
Quasi-static compressive strength (MPa)	40
Friction angle β (degrees)	28
Dilation angle ψ (degrees)	20
K	0.8

Table 4
Parameters used in Johnson–Cook model for reinforcing steel fibers.

Density (g/cm³)	7.8
Young's modulus E (GPa)	203
Poisson's ratio ν	0.28
A (Mpa)	792
B (Mpa)	510
n	0.26
C	0.014
T_{room} (K)	300
T_{melt} (K)	1793
m	1.03
$\dot{\varepsilon}_0$ (s⁻¹)	1
Specific heat (J/kg-K)	477

3.4. Interfaces

Cohesive elements are specified between all bulk elements boundaries with the exception of elements in the fibers, which are assumed to undergo no fracture. The cohesive elements allow for damage initiation and development. The use of a cohesive crack zone for modeling fracture in concrete materials has a long and well-established history, dating back to the 1970s with the work by Hillerborg, Modeer, and Petersson [27]. The use of zero-thickness cohesive elements was established in 1989 by Gens, Carol, and Alonso [28]. A bilinear traction–separation law is adopted to govern the behavior of the cohesive elements [29]. The use of a bilinear traction–separation law to model fracture in concrete materials was first formulated by Petersson [30] in 1981 and has seen extensive use in the time since [31].

The linear-elastic part of the traction–separation law relates the traction vector $\mathbf{t}$ to the element stiffness $\mathbf{K}$ and the separation $\mathbf{u}$ resulting from the traction vector $\mathbf{t}$. This relationship is given by

$$\mathbf{t} = \mathbf{Ku}.\tag{8}$$

The above equation can be expressed in matrix form to indicate coupling between the normal and shear components of the traction–separation relationship, i.e.,

$$\begin{pmatrix} t_n \\ t_s \\ t_t \end{pmatrix} = \begin{bmatrix} K_{nn} & K_{ns} & K_{nt} \\ K_{ns} & K_{ss} & K_{st} \\ K_{nt} & K_{st} & K_{tt} \end{bmatrix} \begin{pmatrix} u_n \\ u_s \\ u_t \end{pmatrix}.\tag{9}$$

Full coupling between normal and shear components in the traction–separation response is represented by the off-diagonal terms. For the purposes of this work, an uncoupled relation is chosen, i.e.,

$$\begin{pmatrix} t_n \\ t_s \\ t_t \end{pmatrix} = \begin{bmatrix} K_{nn} & 0 & 0 \\ 0 & K_{ss} & 0 \\ 0 & 0 & K_{tt} \end{bmatrix} \begin{pmatrix} u_n \\ u_s \\ u_t \end{pmatrix}.\tag{10}$$

Although the linear-elastic part of the response has no coupling between shear and normal components, damage initiation and evolution have a mixed-mode form. Damage initiation follows the quadratic interaction relationship shown in Eq. (11), where t_n is the normal stress in a cohesive element, t_s is the shear stress, and t_n^0 and t_s^0 are the critical values of t_n and t_s, respectively, which represent the cohesive strength. In this paper, both t_s^0 and t_t^0 are assumed to have the same value. Because it is not physically meaningful for compressive tractions to contribute to damage initiation, only non-negative (tensile) normal tractions are considered in the damage initiation rule. This is indicated by the presence of the Macaulay brackets around t_n. Damage is initiated when

$$\left(\frac{\langle t_n \rangle}{t_n^0}\right)^2 + \left(\frac{\langle t_s \rangle}{t_s^0}\right)^2 + \left(\frac{t_t}{t_t^0}\right)^2 = 1.\tag{11}$$
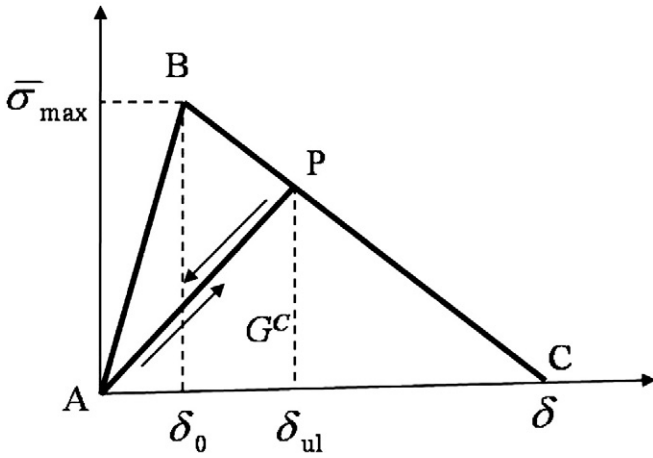
Fig. 3. Bilinear traction–separation law for cohesive elements.

A schematic representation of the bilinear traction–separation law is shown in Fig. 3. Loading initially proceeds from point A to B, at which point softening occurs with increasing strain until failure at a separation of δ.

Once damage is initiated in a cohesive element, the interface follows the mixed-mode fracture criterion of Benzeggagh and Kenane given in Eq. (12) [32]. In this relationship, G_n, G_s, and G_t are the work performed by tractions $L_{fiber} = 10\,mm$, $\phi_{fiber} = 0.4\,mm$, and $\dfrac{L_{fiber} = 10\,mm}{\phi_{fiber} = 0.4\,mm}$, respectively. Δx_0, $\dfrac{\langle H_n \rangle}{\langle P_n \rangle} = 1 + B_n \left(\dfrac{f}{f_o}\right)^{m_n}$, and $\langle P_n \rangle = \dfrac{n(2n)!}{(2^n n!)^2 \sqrt{N/A}}$. are the critical fracture energies in the normal and shear directions, respectively. These quantities are used to determine the degree of damage in a cohesive surface pair. For convenience, the critical fracture energies in the two shear directions are treated as equal (i.e., $\dot{\lambda}$). The criterion is written as

$$G_n^C + \left(G_s^C - G_n^C\right)\left(\frac{G_s + G_t}{G_n + G_s + G_t}\right)^\eta = G^C. \tag{12}$$

There are four interface zones in the model, i.e., paste–paste, quartz–quartz, quartz–paste, and fiber–paste. The constitutive behavior of all cohesive elements modeled in this study follows the same constitutive law; however, the calibration of the traction–separation stiffness, peak traction across the element ($x = \{x_1, x_2, \ldots, x_i, \ldots, x_n\}$), and the normal and shear fracture energies ($\boldsymbol{x}_0$ and $\Delta \boldsymbol{x}_0$) is specific to each type of interface. The parameters for all cohesive relations used in this study are presented in Table 5.

As shown in Table 5, the traction–separation stiffness for cohesive elements along interfaces between the phases and within the bulk phases is a factor of 10^3 times the stiffness of the corresponding bulk elements. This choice has two benefits. First, artificial softening of the model is avoided. Second, the work of separation associated with the linear-elastic portion of the cohesive behavior is minimized, ensuring that the bulk of the work is in the fracture energy, providing

adequate softening in the cohesive response. Although the method of constituent preparation can have a significant influence on the resulting composite fracture toughness [33], only a single set of interface properties are considered in this paper.

3.5. Interfacial contact and friction

After failure of cohesive elements, contact between bulk elements leads to frictional sliding. Contact between element faces is incorporated into the model using the contact algorithm similar to that developed by Camacho and Ortiz [34]. The algorithm identifies free surfaces and fractured surfaces as potential contact surfaces in each time step of the simulation. Nodal coordinates at the end of every time step are used to define master and slave surfaces for the next time step. Nodal displacements are then calculated at the beginning of every time step. The corresponding nodal coordinates are used to check whether nodes of one internally defined surface have penetrated another internally defined surface. If penetration is predicted, then penalty forces of sufficient magnitude are applied to the surfaces in the direction of their normal such that there is contact between them but no interpenetration. For surfaces that are in contact, the Coulomb friction law governs the interfacial friction force. The coefficient of sliding friction for all interfaces is chosen to be 0.6, a typical value for cement-on-cement sliding [35]. It is assumed that the static and dynamic coefficients of friction are the same.
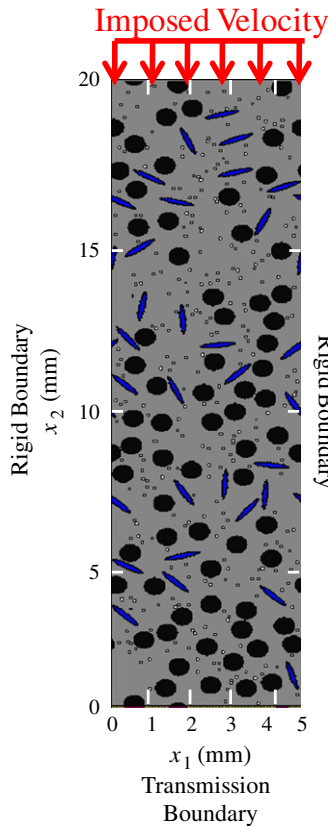
4. Cohesive finite element model

Fig. 4 illustrates the configuration of the computational model along with the loading and constraint conditions. The particular microstructure shown has 10% aggregate, 2.5% porosity, and 2.5% fibers by volume. Compressive loading is created by the imposition of a boundary velocity normal to the top surface. For all calculations, the imposed velocity is 1000 m/s, giving rise to a nominal strain rate of 5×10^4 s^{-1} if the deformation in the whole model was uniform. The calculations consider the first 10 μs of deformation, resulting in a total strain of 30% in the vertical direction. Rigid boundary conditions are applied at the lateral sides of the microstructure, allowing the computations to approximate the overall conditions of uniaxial strain with significant lateral confining stresses.

The cohesive finite element model has a mesh resolution of 33.3 μm/element. In the absence of pores, the mesh consists of 360,000 six-noded triangular prism (type C3D6 in Abaqus) bulk elements and 1,438,800 8-noded (type COH3D8) cohesive elements. Cohesive elements are present at all phase boundaries of all bulk elements; consequently, fracture between the constituent phases can be resolved. Additionally, cohesive elements are present within regions of quartz and matrix bulk elements, allowing for fracture within the quartz and cementitious matrix to be resolved. The cohesive elements also allow fracture energy and subsequent dissipation through interfacial friction to be analyzed. Infinite elements (type CIN3D8) are specified at the bottom to allow stress waves to pass through the material and minimize reflections back into the microstructure. Despite the presence of this transmission boundary, partial reflections are seen in the calculations due to the fact that material properties change during deformations

Table 5
Cohesive element properties for each interface.

Material	Cement	Quartz aggregate	Cement-aggregate interface	Cement-fiber interface
K_n (TPa)	22.9	96.6	22.9	22.9
$K_{s/t}$ (TPa)	9.5	44.7	9.5	9.5
t_n^0 (MPa)	40.0	50.0	10.0	10.0
$t_{s/t}^0$ (MPa)	25.0	40.0	6.0	6.0
G_n^C (J/m^2)	40.0	15.0	5.0	5.0
$G_{s/t}^C$ (J/m^2)	40.0	15.0	5.0	5.0
η	1.45	1.45	1.45	1.45

Fig. 4. Cohesive finite element model for UHPC microstructures with four constituent phases of UHPC, imposed velocity, periodic boundary conditions, cohesive elements, and infinite elements.

Fig. 5. Percent changes in (a) load-carrying and (b) energy-dissipation capacities as mesh size is refined.

and a perfect match of impedance cannot be maintained throughout the duration of the loading events. In this paper, only data prior to the arrival of the stress wave at the bottom is used, therefore, the possible reflection of the stress is irrelevant.

A mesh sensitivity study was performed to determine the accuracy of the chosen mesh resolution of 33.3 μm/element. To this end, a microstructure with 10% aggregate, 0% porosity, and 0% fibers by volume was generated and meshed with resolutions of 100, 66.7, 50, 40, and 33.3 μm/element. The results are shown in the form of the rates of change of the quantities in Fig. 5. Both the load-carrying capacity and the energy dissipated converge fairly rapidly. Refining the mesh resolution beyond 33.3 μm does not add significant benefit. Indeed, the macroscopic response of a brittle material system with cohesive elements has been shown to be insensitive to the exact location of any cracks that develop if the material system allows for all significant potential crack paths [36]. The extensively distributed cohesive elements in the models used in this paper meet this criterion.

5. Results and discussion

After all the microstructures are instantiated, the simulations are performed using the commercial finite element analysis software package Abaqus/Explicit [22].

5.1. Load-carrying capacity

In response to the imposed velocity on the upper surface, a stress wave propagates through the microstructure in the direction parallel to the direction of the imposed velocity. The average normal traction on the upper face of the microstructures (t_n) is taken as a measure of the load carried. The averaging is performed over all elements with nodes on the top face. The traction is averaged at each time step of
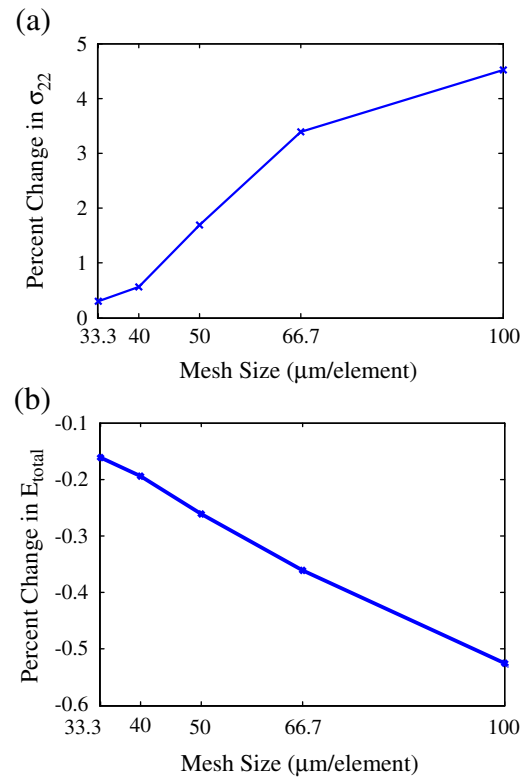
the simulation to provide a single value of the load-carrying capacity at that time. The length of the microstructure in the x_2 direction allows sufficient time for the stress wave to develop so that an accurate representation of the load-carrying capacity can be captured without introducing an artificial response due to interaction with the transmission boundary on the bottom surface.

Fig. 6 shows the normal stress component in the vertical direction in a microstructure having 40% aggregate, 0% porosity, and 10% fibers at three different times in the simulation. The first time is 0.5 μs, which illustrates the initial response of the microstructure. This time is the first point at which stress data are stored in the course of the simulation. The second time is 3.0 μs, which provides a view of the stress in the microstructure at an intermediate time in the simulation. The final time is 6.0 μs. At this point in time, the stress wave has very nearly reached the bottom surface of the microstructure. The implied wave speed is approximately 3.3 km/s. This value agrees reasonably well with the theoretical longitudinal wave speed in cement paste, which is given by $c_d = \sqrt{E(1-\nu)/(1+\nu)(1-2\nu)\rho} \approx 3.3\,\mathrm{km \cdot s^{-1}}$. During the next time step in the simulation, the stress wave reaches the bottom boundary and distorts the results. The microstructure discussed here, with 40% aggregate, 0% porosity, and 10% fibers is the densest microstructure over the range of constituent volume fractions considered and therefore has the highest longitudinal wave speed. As such, the stress wave will also not have reached the bottom surface in any of the other microstructures. Fig. 7 shows the evolution of the average traction on the upper face of a microstructure with 10% aggregate, 0% porosity, and 0% fibers by volume. It can be seen that there are two distinct regions in the response. The first is a linear, rapidly increasing regime. In the second region, where the stress reaches a plateau, granular flow of the cementitious matrix is the dominant deformation mechanism. All microstructures will be compared at 6.0 μs, which provides a comparison during the relatively constant plateau region before the stress wave has reached the bottom surface.
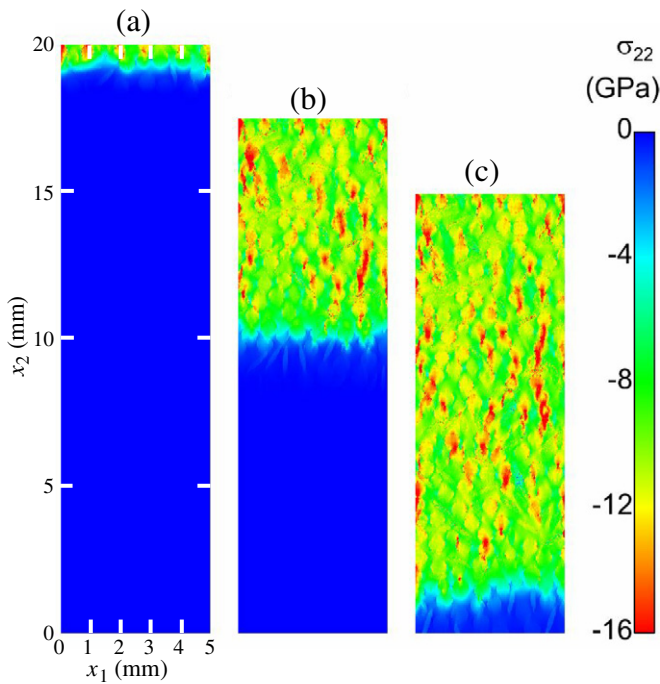
Fig. 6. Propagation of stress wave through a microstructure with 40% aggregate, 0% porosity, and 10% fibers at three different times: (a) 0.5 μs, (b) 3.0 μs, and (c) 6.0 μs.

The load-carrying capacities for all 60 unique microstructures compared in Fig. 8. Four subplots are shown, each corresponding to a different aggregate volume fraction, to more easily present four-dimensional data. Within each plot, the horizontal axes indicate the fiber and porosity volume fractions. The vertical axis shows the normalized load-carrying capacity. The data are normalized to the load-carrying capacity of a microstructure comprised of 100% cementitious matrix. This baseline value is 7.58 GPa. At any time step within the plateau region mentioned above, the traction on the upper face exhibits some degree of variation due to the heterogeneity of UHPC microstructures. However, over the entire plateau region, the traction is relatively constant. Consequently, the load-carrying capacity shown in Fig. 8 is the traction on the upper surface averaged over all time steps in the plateau region. Fibers play a significant role in the load-carrying capacity while the aggregate and porosity play a lesser role. As expected, the microstructure with the largest load-carrying capacity has 40% aggregate, 10% fibers, and 0% porosity. This provides a 38% improvement in the load-carrying capacity as compared to 100% cementitious matrix.
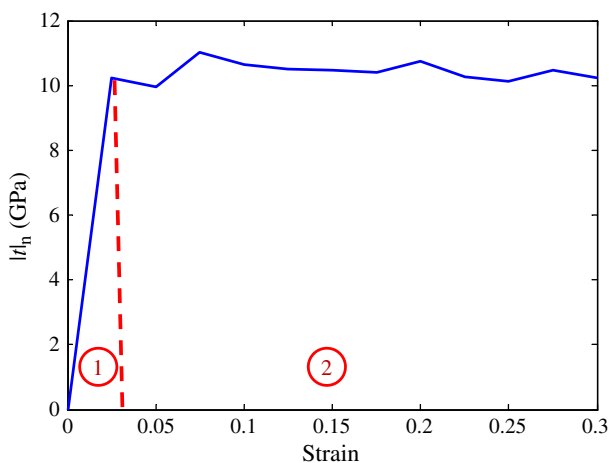

Fig. 7. Evolution of the average normal traction on the upper surface showing two distinct stages for a microstructure with 10% aggregate, 0% fibers, and 0% porosity.

Lammi et al. [15] concluded that there is a synergistic effect between the aggregate and porosity whereby the detrimental effect of porosity is compounded when the aggregate volume fraction is largest. No such trend is found in this analysis. Voids do have a measurable, but minor, effect on the load-carrying capacity. For example, a microstructure with 40% aggregate and 10% fibers experiences a 7% decrease in load-carrying capacity as the porosity is increased from 0% to 5%. This illustrates the need to carefully control porosity in designing UHPC structures.

It can be seen here that increasing aggregate and fiber volume fractions increases the load-carrying capacity. Subsequent sections will show that increasing aggregate and fiber volume fractions also increases the energy dissipation. The fact that the load-carrying capacity increases despite the increase in energy dissipation indicates that the internal damage within the UHPC microstructure does not have a measurable effect on the load-carrying capacity under the loading conditions considered. The foregoing observations suggest that the load-carrying capacity is in reality more of a reaction force at the impact site, and that the load carried is primarily determined by the density of a given microstructure. This is illustrated in Fig. 9, which shows the normalized load-carrying capacity of all 60 microstructures as a function of the average microstructure density. A clear upward trend in the data can be seen. However, the scatter in the data indicates that density alone does not explain the variation in the results. Other factors will be considered in Section 5.3.

Another one of the goals of this study is to assess the attenuation of stress waves in UHPC under dynamic loading. The spatial distribution of the stress component in the vertical direction in microstructures at the extremes, or "corners" in Fig. 1, of the simulated parametric ranges of microstructures can be seen in the eight plots in Fig. 10. This figure shows the stress at 0.5 μs, 2.0 μs , and 4.0 μs. The preceding analysis showed that the load-carrying capacity increases with increasing aggregate and fiber volume fractions, despite the fact that they also serve to increase the energy dissipation as well. However, the load-carrying capacity is measured in this study as the traction on the upper surface of a microstructure. Although there is no attenuation of this load, there may be attenuation within the microstructures. Fig. 10, however, shows that there is no appreciable attenuation of the stress wave over the distance analyzed even as it traverses the microstructure. Although there is moment-to-moment fluctuation, the stress remains relatively constant throughout the microstructure. The fluctuation is due to the heterogeneity of the microstructure. Over the length and time scales considered in this study, the stress throughout a microstructure is governed more by the material's short-term elastic response.

5.2. Energy dissipation

Three modes of energy dissipation are tracked through the course of the simulations, i.e., plastic dissipation due to inelastic deformation in the steel fibers and granular flow of the cementitious paste, damage due to fracture and distributed cracking, and friction at cracked interfaces. More detailed descriptions of the three modes of energy dissipation are provided by Lammi et al. [15] and will be omitted here.

5.2.1. Total energy dissipation

The total energy dissipation is the sum of the three modes of energy dissipation, but each mode does not play an equal role. The exact proportion of energy dissipated by each mode depends on the volume fractions of the constituents. However, some general observations can be made. Fig. 11 shows the evolution of the energy dissipation components in four individual microstructures. It can be seen that increasing porosity and fiber volume fractions increase the portion of energy dissipation attributable to friction but decreases the portion attributable to inelastic deformation. Fig. 11(a) shows porosity and fiber volume fractions of 0%, while Fig. 11(b) shows porosity and fiber volume fractions of 5% and 10%, respectively. The vertical axis on these plots has been normalized
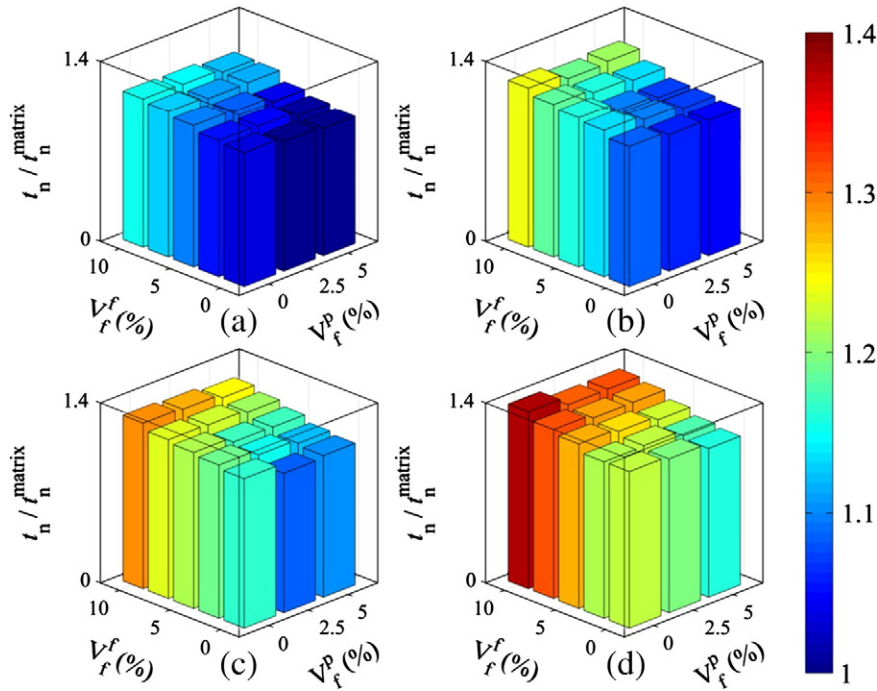
Fig. 8. Normalized load-carrying capacity for all microstructures at four different aggregate volume fractions: (a) 10%, (b) 20%, (c) 30% and (d) 40%.

such that the sum of the three energy dissipation components is exactly unity at a strain of 0.3. The two plots appear similar, but there are several differences that arise due to the different volume fractions of the constituents. At a strain of 0.3, inelastic deformation, friction, and fracture contribute 88.1%, 11.7%, and 0.2%, respectively, of the total energy dissipation in the first microstructure. In the second microstructure, inelastic deformation, friction, and fracture contribute 84.9%, 15.0%, and 0.1%, respectively, of the total energy dissipation. Although the presence of fibers and porosity is seen here to decrease the portion of energy dissipation due to inelastic deformation, Section 5.2.4 will show that fibers and porosity in fact increase the nominal value of the plastic component of energy dissipation.

The figure also shows that increasing the aggregate volume fraction increases the portion of energy dissipation attributable to friction but decreases the portion attributable to plastic deformation. In Fig. 11(c), inelastic deformation, friction, and fracture contribute 91.3%, 8.9%, and 0.2%, respectively, of the total energy dissipation. In Fig. 11(d), inelastic

Fig. 9. Normalized load-carrying capacity as a function of the overall density of the materials.

deformation, friction, and fracture contribute 79.2%, 20.6%, and 0.2%, respectively, of the total energy dissipation. In order to increase the overall energy dissipation, emphasis should be placed on enhancing frictional and plastic work in the microstructure. Changing either of these by a given percentage will have a far larger effect on the overall total than changing the damage energy by the same percentage.

Comparing the total energy-dissipation in all 60 microstructures necessitates a more concise format. Fig. 12(a) shows the total energy-dissipation capacity in microstructures with 40% aggregate. The data for other aggregate volume fractions show similar trends. The horizontal axes indicate the fiber and porosity volume fractions. The vertical axis shows the normalized energy-dissipation capacity. In this figure, E_d, E_f, and E_p represent the energy dissipated through damage and fracture, through interfacial friction, and through plastic deformation, respectively. The data are normalized by the total energy dissipation of a baseline case, a microstructure comprised of 100% cementitious matrix. The values correspond to a simulation time of 6.0 μs.

As predicted, increasing the volume fraction of all three constituent phases serves to increase the total energy dissipation. However, the addition of a small amount of aggregate alone decreases the total energy dissipation. Specifically, the microstructure with 10% aggregate and no fibers or porosity has an energy-dissipation capacity of 84% of the baseline case. Even the microstructure with 40% aggregate and no fibers or porosity has an energy-dissipation capacity just 3% higher than that of the baseline case. Despite the fact that aggregate alone does little to improve the energy-dissipation capacity, and in fact diminishes it at low volume fractions, the aggregate has a synergistic effect with porosity. That is, increasing porosity provides more of a benefit to the energy dissipation at larger aggregate volume fractions. In particular, at 10% aggregate and 0% fibers, increasing the porosity from 0% to 5% increases the energy dissipation by 14%, relative to the baseline. At 40% aggregate, however, the same increase in porosity yields an energy dissipation 22% larger than that of the baseline.

Finally, the total energy dissipation in all microstructures is less than 10% of the total external work. This is likely the reason that the stress does not exhibit measurable attenuation as discussed earlier in Section 5.1. This is not to say that UHPC structures are incapable of attenuating an applied load. Rather, larger size and time scales, which
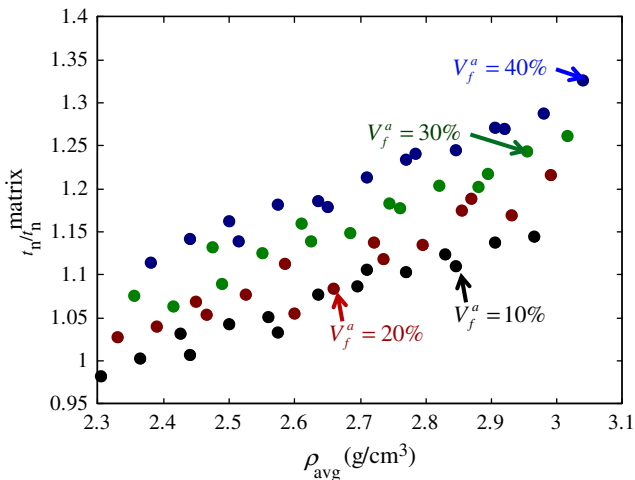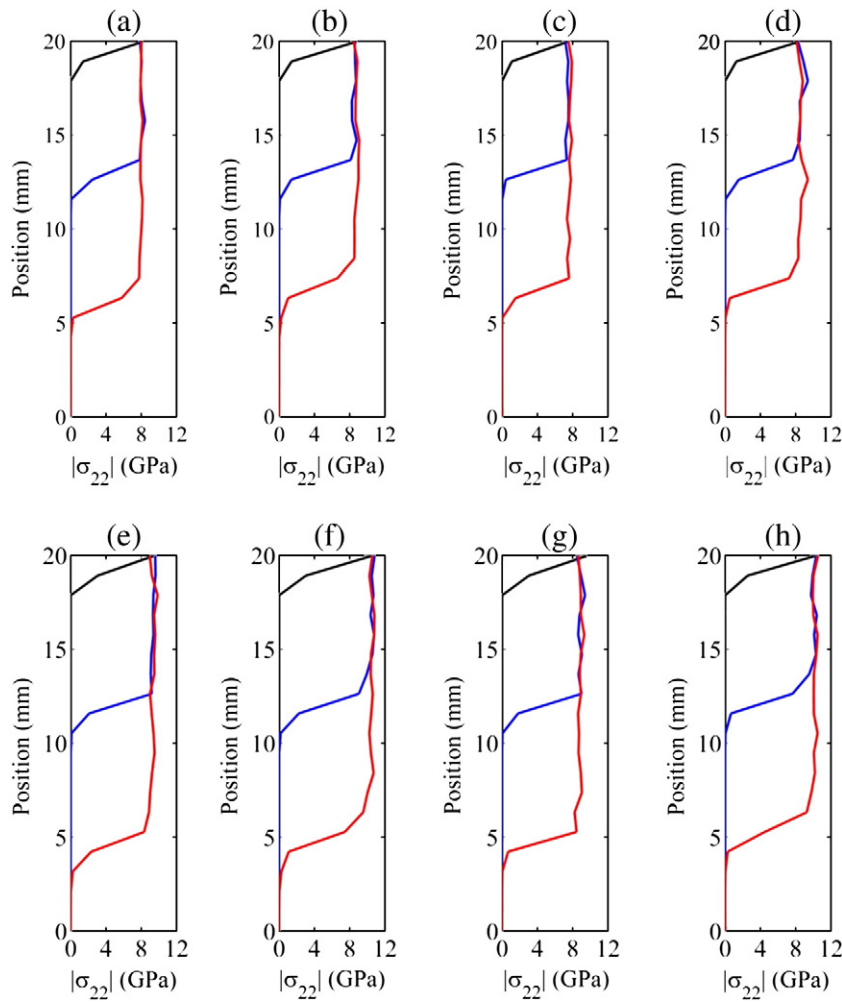
Fig. 10. Stress propagation in microstructures at the eight extremes of the design space at 0.5 μs, 2.0 μs, and 4.0 μs: (a) 10% aggregate, 0% porosity, 0% fibers; (b) 10% aggregate, 0% porosity, 10% fibers; (c) 10% aggregate, 5% porosity, 0% fibers; (d) 10% aggregate, 5% porosity, 10% fibers; (e) 40% aggregate, 0% porosity, 0% fibers; (f) 40% aggregate, 0% porosity, 10% fibers; (g) 40% aggregate, 5% porosity, 0% fibers; (h) 40% aggregate, 5% porosity, 10% fibers.

would allow for a larger percentage of the external work to be dissipated, would likely be necessary for the stress to show signs of attenuation. The low percentage of external work dissipated may also be due to the rigid lateral boundary conditions, which restrict motion in the x_1 (horizontal) direction. Identical simulations with traction-free boundary conditions dissipate up to approximately 20% of the total external work. Nonetheless, the trends in the data agree with experimental findings. Increased porosity and fibers allow for a greater percentage of the external work to be dissipated.

The unique nature of the cohesive finite element model presented herein allows for the energy dissipation to be broken down into three constituent components, i.e., damage through interface fracture, inelastic deformation and granular flow of the cementitious paste, and interfacial friction along cracked interfaces. The components of the total energy dissipation will be discussed in more detail below, beginning with the energy dissipated through damage and fracture of interfaces, then the energy dissipated through friction between fractured interfaces, and ending with the energy dissipated through inelastic deformation.

5.2.2. Energy dissipated through interface fracture

Fig. 12(b) shows the energy dissipation through interface damage and fracture in microstructures having 40% aggregate. Data for other aggregate volume fractions show similar trends. Note that nearly all microstructures dissipate less energy through damage than the baseline case. It is not until volume fractions of 40% aggregate and 5%

porosity that more energy is dissipated through damage than in the baseline microstructure. Specifically, the microstructure with 40% aggregate, 5% porosity, and 0% fibers dissipates 15% more energy than the baseline case. As fibers are added, the energy dissipated through damage decreases. At 40% aggregate, 5% porosity, and 10% fibers, the energy dissipated through damage is 97% of the damage dissipation in the baseline case.

The porosity has a synergistic effect with the aggregate on the energy dissipated through interface damage, similar to the trend observed in the total energy dissipation. That is, the benefit of porosity increases with increasing aggregate volume fractions. For example, at 10% aggregate and 0% fibers, increasing the porosity from 0% to 5% increases the energy dissipated through interface damage and fracture by 21% with respect to the baseline. At 40% aggregate, the same increase in porosity yields a 35% increase in the energy dissipated through interface damage and fracture, relative to the baseline.

Fibers and porosity have a competing effect on the energy dissipated through interface damage and friction. The benefit of porosity diminishes with increasing fiber volume fractions. For example, at 10% aggregate, increasing the porosity from 0% to 5% can increase the energy dissipated through damage by as much as 21% in the absence of fibers, or as little as 17%, in the presence of a 10% fiber volume fraction. This competing effect is even more pronounced at high aggregate volume fractions. For example, at 40% aggregate, increasing the porosity from 0% to 5% can increase the energy dissipated through damage by up to
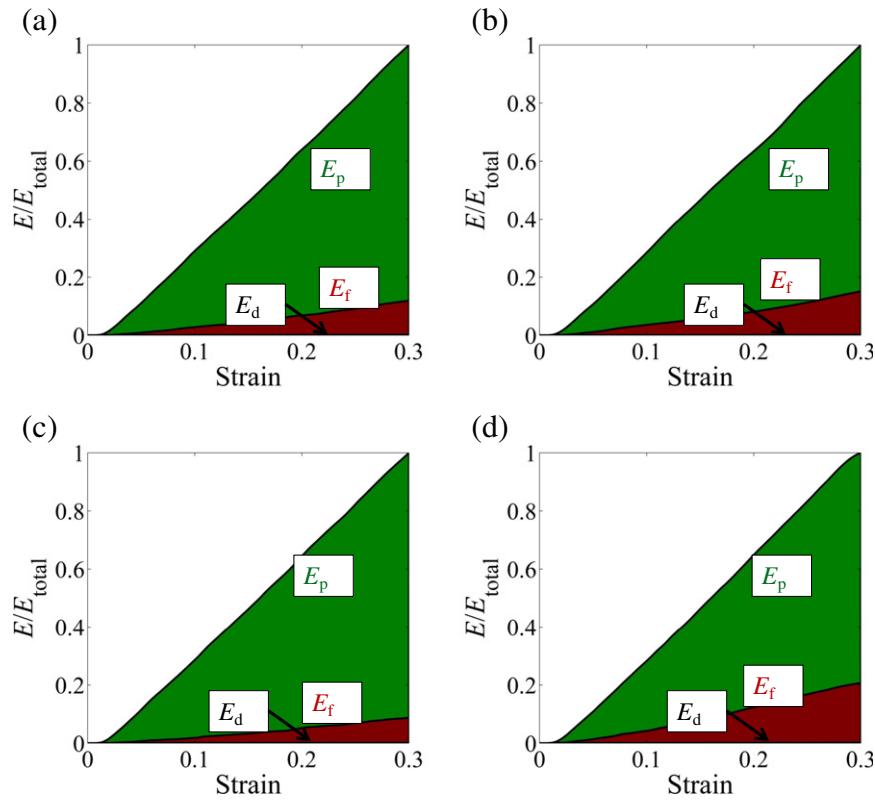
Fig. 11. Components of the total energy dissipated as a function of strain for microstructures with (a) 20% aggregate, 0% porosity, 0% fibers, (b) 20% aggregate, 5% porosity, 10% fibers, (c) 10% aggregate, 0% porosity, 0% fibers, and (d) 40% aggregate, 0% porosity, 0% fibers.

35% in the absence of fibers, or as little as 25% in the presence of a 10% fiber volume fraction.

The energy dissipated through damage and fracture is by definition due in part to the energy dissipated in the pre-failure elastic softening of interfaces. This energy dissipation component, therefore, does not provide an accurate representation of the degree of cracking. Two common metrics for assessing the extent of cracking in solids are the scalar crack density parameter and the crack density tensor [37,38]. The
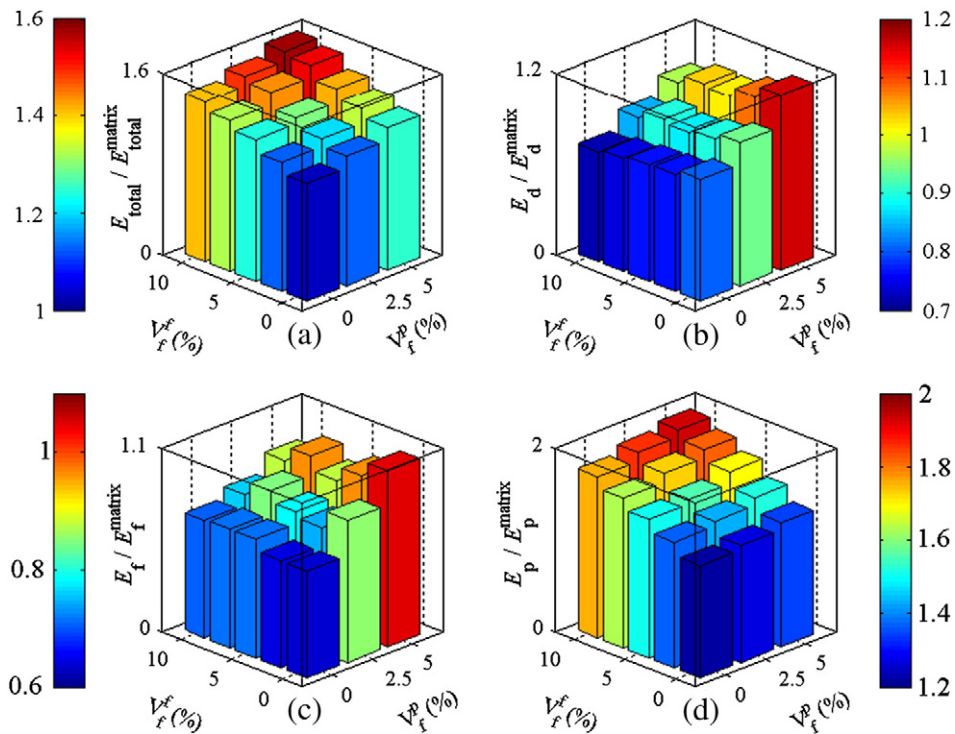
Fig. 12. Normalized energy dissipations at 6.0 μs for microstructures with 40% aggregate: (a) total energy dissipation, (b) energy dissipation through interface damage and fracture (c) energy dissipation through friction between crack surfaces, and (d) energy dissipation through inelastic deformation.

two-dimensional scalar crack density D_A is given by $D_A = \frac{1}{A}\sum_{k=1}^{N} l_k^2$, where A is the 2D area of averaging, l_k is the half-length of the kth crack, and N is the total number of cracks. More useful than the scalar parameter is the crack density tensor, which provides information about the degree of anisotropy of cracking in a solid. The components of the crack density tensor are given by $D_{ij} = \frac{1}{A}\sum_{k=1}^{n} l_k^2 \boldsymbol{n}_i^k \boldsymbol{n}_j^k$ where $\boldsymbol{n}^k$ is the unit vector normal to the kth crack. Provided the directional distribution of damage is adequately represented by a second rank tensor, the relationship between the scalar crack density parameter and the tensor is simply $D_A = tr(\mathbf{D})$. The significance of the crack density tensor is that it provides insight into both the extent of cracking and the degree to which it is anisotropic, which can influence the material's effective elastic properties if the cracking has a preferred orientation. For purely vertical cracking, the corresponding crack density tensor only has one non-zero component in the (1,1) position. For purely horizontal cracking, the only non-zero component of the crack density tensor is in the (2,2) position, for example.

The crack density tensor is calculated for each microstructure at each time step of the analysis. Because each volume fraction of phases within a microstructure results in an associated second rank crack density tensor, the space of damaged microstructures becomes a five-dimensional data set. However, because of the inherent difficulty in visualizing such multi-dimensional data, the results will show the scalar crack density parameter. Fig. 13 shows the scalar crack density parameter φ in all 60 microstructures. It can be seen that the constituent phase with the greatest influence on the scalar crack density parameter is porosity. For example, at 40% aggregate and 0% fibers, increasing the porosity from 0% to 5% increases the scalar crack density by 193%. As with the energy dissipated through damage and fracture, porosity and fibers have competing effects on the crack density. Increasing the porosity serves to drastically increase the crack density. Fibers serve to not only decrease the scalar crack density, but also to diminish the effect of porosity. For example, the 193% increase in the scalar crack density discussed previously can be lowered to 158% when the microstructure has a fiber volume fraction of 10%

instead of 0%. This is indicative of the ability of fibers to arrest the crack development facilitated by porosity.

The crack density is intimately related to the energy dissipated through interface damage and fracture. The scalar crack density parameter quantifies the extent or magnitude of cracking within a material. It can be regarded as a normalized average crack length. The energy dissipated through damage and fracture is the product of a cracked interface's fracture energy and its area. Thus, the crack density is directly proportional to the energy dissipated through fracture, and the constant of proportionality is equal to the average interface fracture energy. Fig. 14 shows the energy dissipated through interface damage and fracture along with the corresponding scalar crack density parameter as a function of strain in microstructures having 0% fiber and 0% porosity. The blue curves represent the energy dissipation, while the red curves represent the scalar crack density parameter. The line style (dashed, dotted, etc.) represents different porosity volume fractions. As the energy dissipation rises, so too does the crack density.

5.2.2.1. Spatial distribution of energy dissipated through interface fracture. The previous set of results shows the cumulative energy dissipated through interface damage and fracture in the entire microstructure. It is also of interest to investigate how the energy dissipation is distributed throughout the microstructure. In particular, the rate of energy dissipation through damage as a function of vertical position in the microstructure can provide insight into regions that have the most influence on the total energy dissipation.

Fig. 15 shows the spatial distribution of the rate of energy dissipation through interface damage at three instants in time, i.e., 0.5 μs, 2.0 μs, and 4.0 μs. Eight sub-plots are shown, each corresponding to a microstructure at the corners of the 3D parameter space. The vertical axes correspond to vertical position within a microstructure. The horizontal axes show the rate of energy dissipation through interface damage. The rate is normalized to the applied external power for a given microstructure. A number of trends should be noted in the two aforementioned plots. First, the figures show distinct peaks.
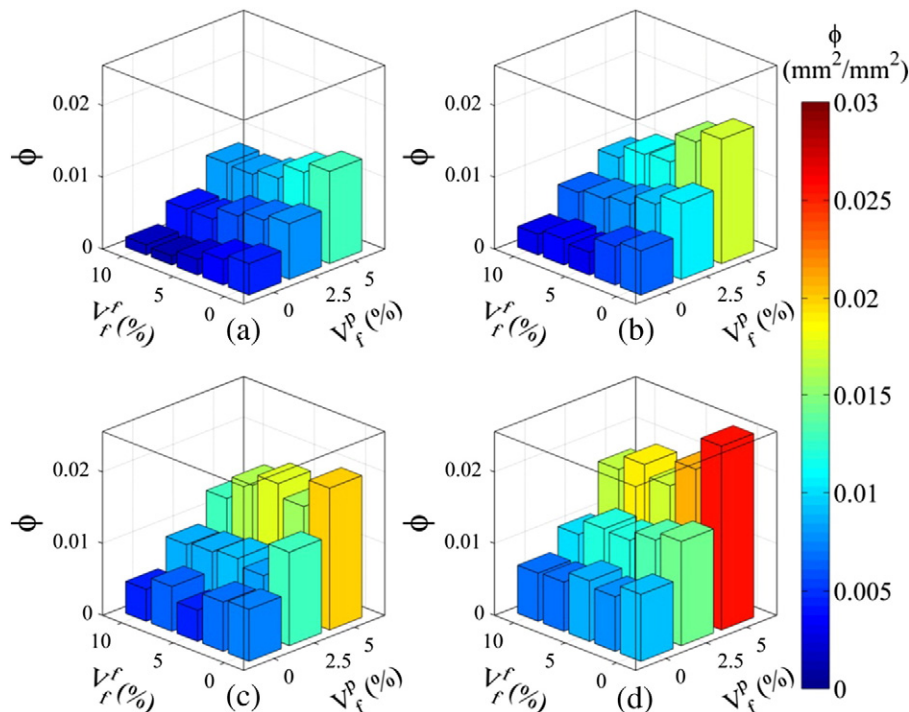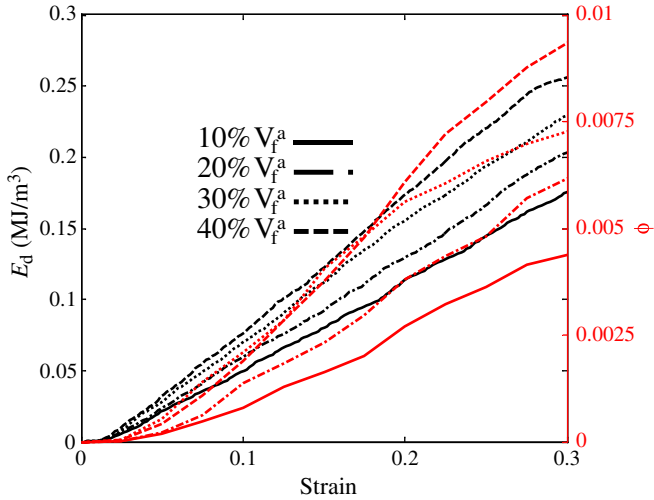

Fig. 13. Scalar crack density parameter at 6.0 μs for all 60 microstructures with four different aggregate volume fractions: (a) 10%, (b) 20%, (c) 30%, and (d) 40%.
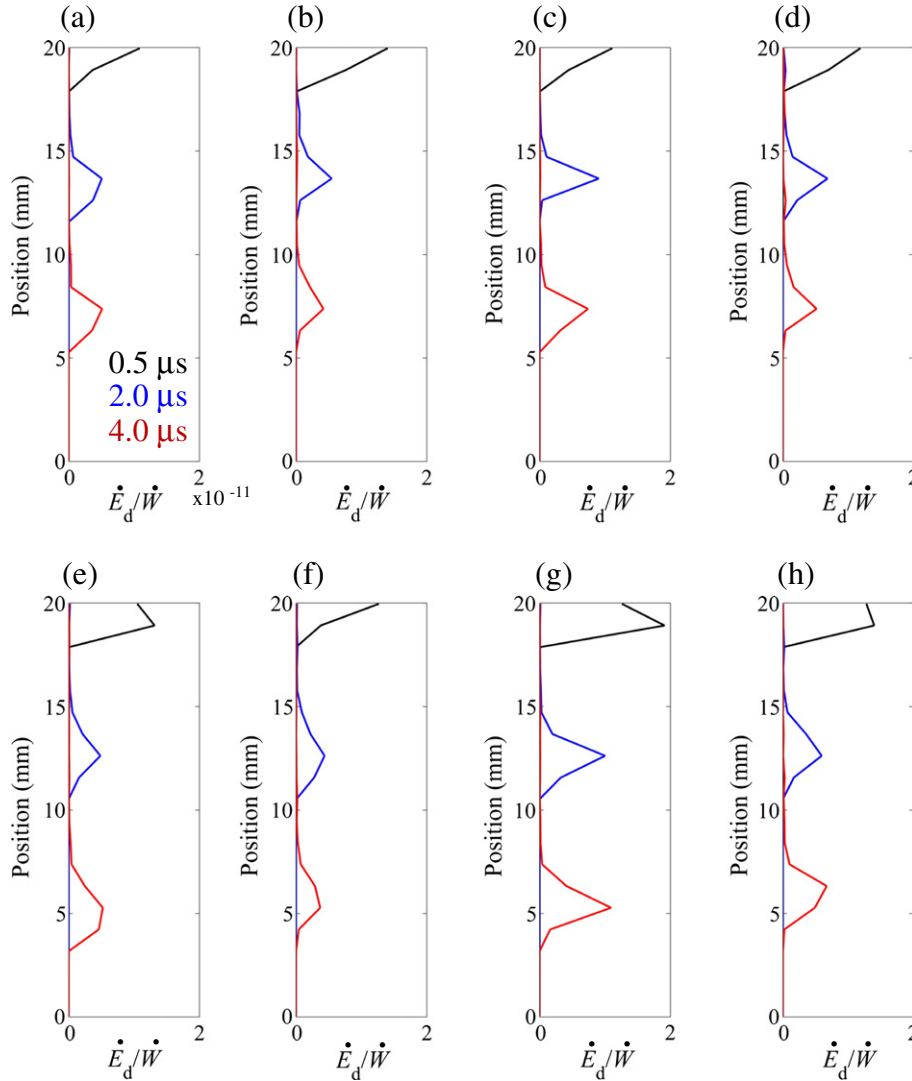
Fig. 14. Energy dissipated through interface damage and fracture along with the corresponding scalar crack density parameter as a function of strain in microstructures having 0% fibers and 0% porosity over a range of aggregate volume fractions.

These peaks correspond to the front of the propagating stress wave. Behind the stress wave, the rate of energy dissipation is on the order of 10^3 times smaller than the rate on the cusp of the wave front. This suggests that as the stress wave propagates through the microstructure, damage and fracture primarily occur at the wave front. The figures also corroborate the result shown in the 3D bar charts in Fig. 12(b). The peaks in the bottom row of sub-plots of Fig. 15, which show data from microstructures with 40% aggregate, are clearly higher than the peaks in the top row of sub-plots, which show data from microstructures with only 10% aggregate. This agrees with the previous finding that higher aggregate content leads to higher energy dissipation due to interface damage.

5.2.3. Energy dissipated through interfacial friction

Fig. 12(c) shows the energy dissipation through friction between fractured interfaces in microstructures with 40% aggregate. The data for other aggregate volume fractions show similar trends. This figure shows many similarities to the data shown in Fig. 12(b) that are discussed in Section 5.2.2. This is expected; friction along crack faces cannot occur until fracture has occurred. Constituents that

Fig. 15. Spatial distributions of the normalized rate of energy dissipation through interface damage in microstructures at the eight extremes of the design space at 0.5 μs, 2.0 μs, and 4.0 μs: (a) 10% aggregate, 0% porosity, 0% fibers; (b) 10% aggregate, 0% porosity, 10% fibers; (c) 10% aggregate, 5% porosity, 0% fibers; (d) 10% aggregate, 5% porosity, 10% fibers; (e) 40% aggregate, 0% porosity, 0% fibers; (f) 40% aggregate, 0% porosity, 10% fibers; (g) 40% aggregate, 5% porosity, 0% fibers; (h) 40% aggregate, 5% porosity, 10% fibers.

contribute to interface fracture will also contribute to frictional dissipation.

As with the crack density and damage energy dissipation, porosity and fibers have competing effects on the frictional energy dissipation. Increased porosity leads to higher energy dissipation, but this influence is mitigated by the presence of fibers. For example, at an aggregate volume fraction of 10% without any fibers, increasing the porosity from 0% to 5% increases the frictional energy dissipation by 31% relative to the baseline case. However, when the fiber volume fraction is 10%, the same increase in porosity yields only a 21% increase in the frictional energy dissipation. While this is still a large increase, it is significantly less than the increase observed when the fiber volume fraction is 0%. This suggests that at low porosity and low fiber volume fractions, increasing the porosity is the best means of increasing the frictional energy dissipation.

A key difference between the trends in energy dissipated through interface fracture and friction is that increasing fiber volume fractions decrease the energy dissipated through fracture at all porosity volume fractions. In contrast, increasing fiber volume fractions *increase* the energy dissipated through friction at low porosity volume fractions, but *decrease* the energy dissipated through friction at high porosity volume fractions. This indicates that the role of fibers in the energy dissipation process shifts depending on the amounts of the other constituents. At low porosity volume fractions, fibers serve to arrest crack propagation and also generate friction with the cementitious matrix. At high volume fractions of porosity, cracking becomes more extensive and the ability of fibers to arrest crack propagation constrains frictional sliding.

5.2.4. Energy dissipated through inelastic deformation

Fig. 12(d) shows the energy dissipation through inelastic deformation in microstructures with 40% aggregate. Data for other aggregate volume fractions show similar trends. Unlike the other two components of energy dissipation, where large volume fractions of the constituents are necessary to generate energy dissipation values in excess of those of the baseline case, the energy dissipated through inelastic deformation is higher than that of the baseline cases for all volume fractions considered. Specifically, at 10% aggregate, 0% porosity, and 0% fibers, the plastic energy dissipation is 15% higher than that of the baseline case. Increasing the volume fraction of any of the constituents increases the plastic dissipation.

The fiber volume fraction has a substantial influence on the energy dissipated through inelastic deformation. At all levels of aggregate and porosity, increasing the fiber volume fraction from 0% to 10% increases the energy dissipation through inelastic deformation by over 45% relative to the baseline case. The aggregate and porosity phases have only a slight influence on the amount of energy dissipated through inelastic deformation. At a given fiber volume fraction, changing either the aggregate or porosity volume fractions within the range considered changes the plastic energy dissipation by less than 10% relative to the baseline.

The effect of the fibers and porosity on the energy dissipated through inelastic deformation is shown in Fig. 16. This figure compares the equivalent plastic strains in three microstructures with a common aggregate fraction of 10%, but different fiber and porosity volume fractions. Fig. 16(a) shows a microstructure with 0% fibers and 0% porosity, Fig. 16(b) shows a microstructure with 10% fibers and 0% porosity, and Fig. 16(c) shows a microstructure with 0% fibers and 5% porosity. The color map scales are identical in the images to facilitate direct comparison. Fig. 16(a) shows the highest levels of plastic strain concentrated above and below the quartz grains. This is consistent with the theoretical prediction for spherical inclusions in an elasto-plastic matrix. Fig. 16(b) shows substantially larger plastic strains than those Fig. 16(a). The areas of highest plastic strain correspond to fiber locations. This is indicative of the significant effect of fibers on the inelastic deformation and the slight influence from porosity. Fig. 16(c) shows elevated plastic strains around collapsed voids.

5.2.4.1. Spatial distribution of energy dissipated through inelastic deformation.
The previous set of results show the cumulative energy dissipated through inelastic deformation in the entire microstructure. It is also of interest to understand how the energy dissipation is distributed throughout the microstructure. In particular, the rate of plastic energy dissipation as a function of vertical position in the microstructure can provide insight into regions that have the most influence on the total energy dissipation.

Fig. 17 shows the spatial distribution of the rate of energy dissipation through interface damage at 0.5 μs, 2.0 μs, and 4.0 μs after the beginning of loading. Eight sub-plots are shown, each corresponding to a microstructure at the corners/limits of range of the parametric study. The vertical axes correspond to vertical position within a microstructure. The horizontal axes show the rate of energy dissipation through plastic deformation. The rate is normalized to the applied external work input rate for a given microstructure. This input rate is on the order of 10^5 W. To obtain a complete picture of the spatial distribution of the energy dissipation, it is necessary to consider different times. Several trends can be identified from these plots, all of which are similar to the trends previously observed in the distributions of the energy dissipated through interface damage. First, the figures show distinct peaks. These peaks correspond to the front of the propagating stress wave. Behind the stress wave front, the rate of energy dissipation is on the order of 10^3 times smaller than the rate on the cusp of the wave front, suggesting that, as the stress wave propagates through the microstructure, inelastic deformation occurs primarily at the wave front and behind the front, little deformation occurs. In this regard, the spatial distribution of energy dissipation through inelastic deformation is similar to the distribution of energy dissipation through interface damage.

5.3. Microstructure performance-relation maps

The preceding discussion has focused on the load-carrying capacity and components of energy-dissipation capacity, and its individual components. In particular, the results of parametric studies have been shown in a format wherein the response variables are functions of the volume fractions of constituent phases. However, the process of materials' design flows in the opposite direction, from the top–down. Performance objectives are specified, and then the necessary material attributes are identified. Structure–property/response trends shown in Fig. 18, which relate the load-carrying and energy-dissipation capacities to the volume fractions of constituents.

In Fig. 18(a), the vertical axis shows a combined performance metric defined as the product of the energy-dissipation capacity and the
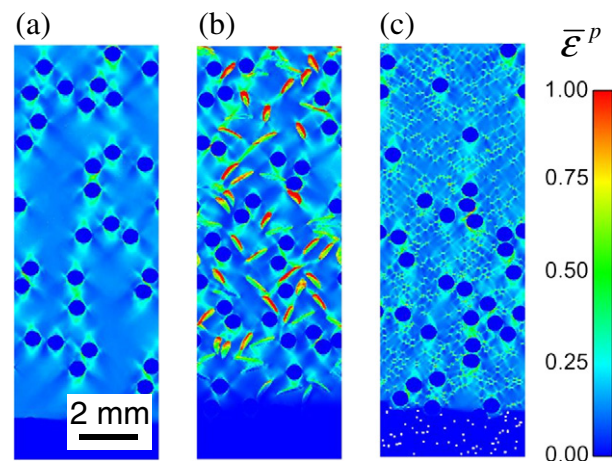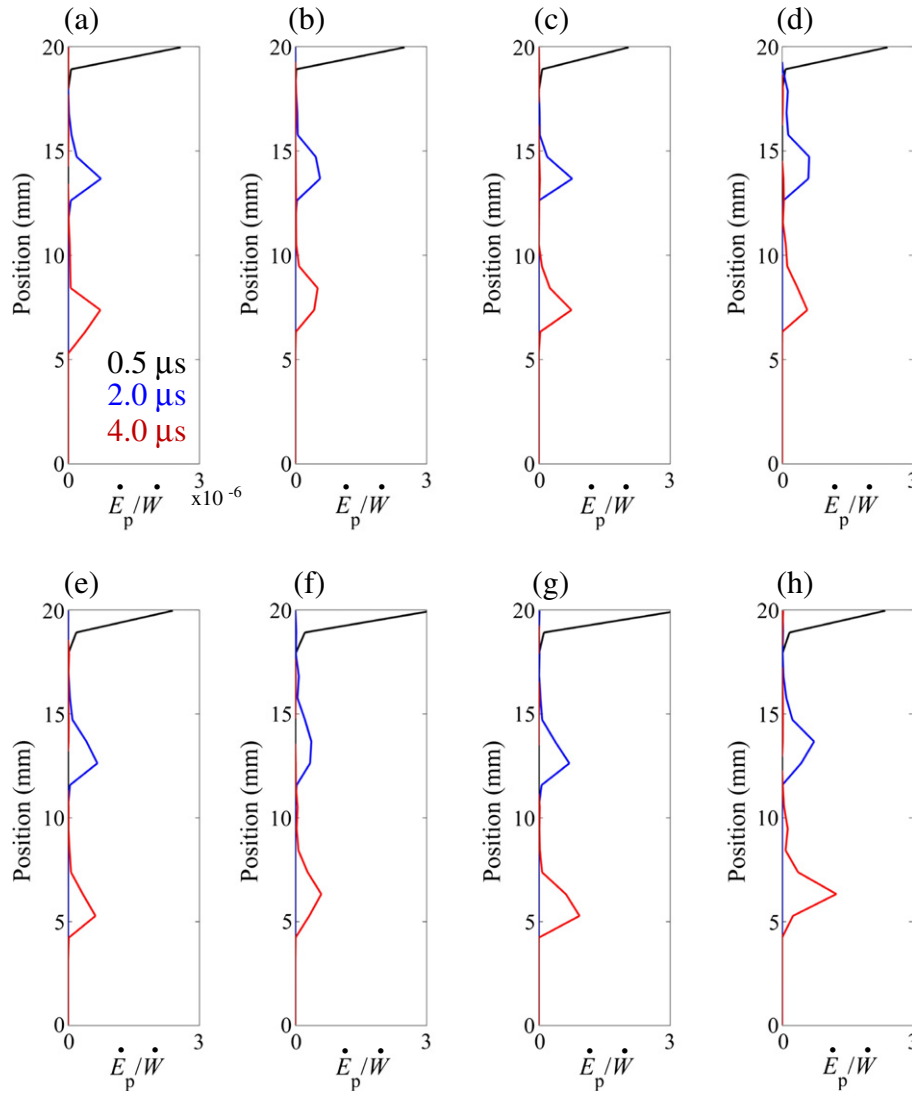

Fig. 16. Distributions of equivalent plastic strain at 6.0 μs in microstructures with 10% aggregate and (a) 0% porosity, 0% fibers, (b) 0% porosity, 10% fibers, and (c) 5% porosity, 0% fibers.

Fig. 17. Spatial distributions of the normalized rate of energy dissipation through inelastic deformation in microstructures at the eight extremes of the design space at 0.5 μs, 2.0 μs, and 4.0 μs: (a) 10% aggregate, 0% porosity, 0% fibers; (b) 10% aggregate, 0% porosity, 10% fibers; (c) 10% aggregate, 5% porosity, 0% fibers; (d) 10% aggregate, 5% porosity, 10% fibers; (e) 40% aggregate, 0% porosity, 0% fibers; (f) 40% aggregate, 0% porosity, 10% fibers; (g) 40% aggregate, 5% porosity, 0% fibers; (h) 40% aggregate, 5% porosity, 10% fibers.

load-carrying capacity. Here, the energy-dissipation capacity is expressed as the total energy dissipation normalized by the total external work; that is, the total work dissipated as a fraction of the total work imparted into the material. The load-carrying capacity is expressed as the traction on the upper surface of a given microstructure normalized by the traction on the upper surface of a microstructure comprised of
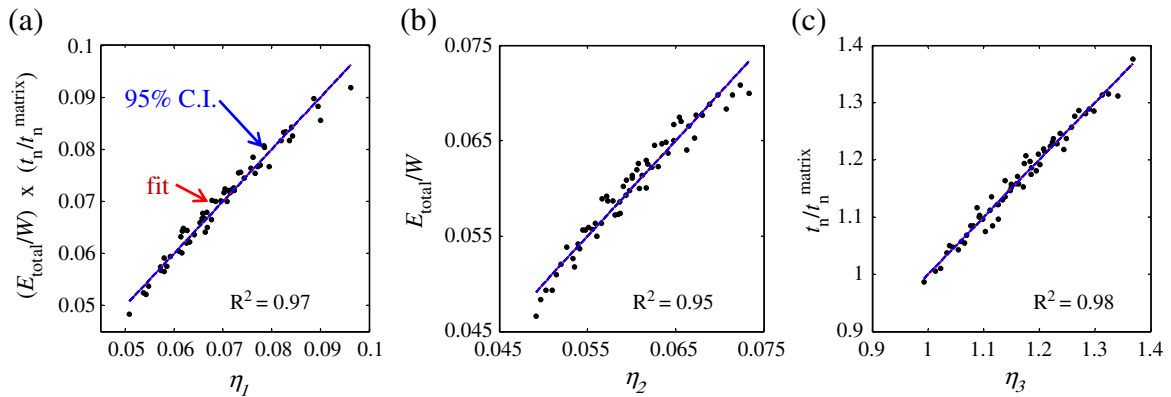
Fig. 18. Microstructure performance relations relating (a) energy-dissipation capacity and load-carrying capacity and volume fractions of constituents through parameter η_1, (b) energy-dissipation capacity to volume fractions of constituents through microstructure parameter η_2, and (c) load–carrying capacity to volume fractions of constituents through microstructure parameter η_3.

100% cementitious matrix. The horizontal axis is a parameter that depends on the volume fractions of the constituents in microstructures. This parameter is obtained through a linear regression analysis and takes the form of

$$\left(\frac{E_{Total}}{W}\right) \times \left(\frac{t_n}{t_n^{matrix}}\right) = \eta_1 = \frac{0.048}{\left(1-V_f^a\right)^{0.47}\left(1-V_f^f\right)^{3.0}\left(1-V_f^p\right)^{2.6}}, \quad (13)$$

which provides the best description of the correlation among dissipation, loading carried, and microstructure.

This chart allows the identification of specific material microstructure designs for any given combination of desired load-carrying capacity and energy-dissipation. It is useful for identifying microstructure settings that may meet desired performance objectives and allows the trade-offs between conflicting requirements to be explored. It should be noted, however, that such maps are only applicable to loading under conditions of nominally uniaxial strain and consider only the volume fractions of constituents as design variables. The relation clearly captures the trade-offs between energy dissipation and strength clearly, i.e., increasing the load-carrying capacity will likely reduce the energy-dissipation capacity.

Fig. 18(b) relates the energy-dissipation capacity to microstructure. Like the relation in Fig. 18(a), the parameter that provides the best description of the correlation between the dissipation and microstructure is

$$\frac{E_{Total}}{W} = \eta_2 = \frac{0.049}{\left(1-V_f^a\right)^{0.09}\left(1-V_f^f\right)^{1.81}\left(1-V_f^p\right)^{3.38}}. \quad (14)$$

With all other parameters fixed, increasing any of the three constituents increases the energy dissipation capability of the material, with porosity having the most significant influence followed by the fibers and then the aggregate.

Fig. 18(c) relates the load-carrying capacity to the volume fractions of the constituents. The parameter that provides the best description of the correlation between the load carried and microstructure is

$$\frac{t_n}{t_n^{matrix}} = \eta_3 = \frac{0.99\left(1-V_f^p\right)^{0.80}}{\left(1-V_f^a\right)^{0.38}\left(1-V_f^f\right)^{1.2}}. \quad (15)$$

This relation highlights the fact that fibers have the most influence on the load-carrying capacity, and the correlation is positive. Porosity is the next most influential constituent, and the correlation is negative. Finally, aggregate has the least influence, and the correlation is positive.

The relations in Eqs. (13), (14) and (15) correspond to the design space in Fig. (1) for which the ranges the input variables are $10\% \le V_f^a \le 40\%$, $0\% \le V_f^f \le 10\%$, and $0\% \le V_f^p \le 5\%$. Note that the parameters η_1, η_2, and η_3 are functions of the same microstructural information or

attributes. These parameters represent three different ways of weighing the attributes for the different performance metrics, which are not fully independent of each other. Specifically, $\eta_1 \approx \eta_2\eta_3$, suggesting that, for example, the maximization of the both energy-dissipation and load-carrying capabilities requires proper choices of the volume fractions of fiber, aggregate and voids by iteratively fixing either η_1 or η_2 while changing the other. Also, note that because of the nature of the parametric expressions, the relationship between volume fractions of the constituents and the parameters is not one-to-one. That is, multiple microstructural compositions can yield the same parameter value. Fig. 19 shows the values of the microstructure performance parameters taken on by the whole range of microstructure instantiations analyzed. Each point in Fig. 18(a)–(c) represents one of the 60 unique combinations of volume fractions of the constituents. The color of each point corresponds to the value of the parameter as indicated by the color scale legend. The lowest values of η_1 are seen at low volume fractions of aggregate, fibers, and porosity. Microstructures with high aggregate, high fiber, and low porosity contents show parameter values similar to microstructures with high aggregate, low fiber, and high porosity contents. Parameter η_2 shows similar relationships. Microstructures with high aggregate and high fiber volume fractions show the highest values of η_3, with only a minor influence from porosity. Microstructures with low aggregate and low fiber volume fractions show the lowest values of η_3.

The microstructure–performance relations can be used to inform materials' design with the caveat that they should only be used for the microstructural settings considered in this study: high-rate compressive loading with constituent sizes as noted in Table 2 and volume fractions in the range of 10% to 40% aggregate, 0% to 10% fibers, and 0% to 5% porosity. Within this range of constituent volume fractions, the dissipation and load parameters can vary independently of each other. This can be seen in Fig. 20, which shows surfaces of constant η_2 in Fig. 20(a) and surfaces of constant η_3 in Fig. 20(b). For a fixed value of the dissipation parameter, the optimum value of the load parameter is achieved by decreasing porosity, increasing aggregate, and increasing fibers in the proportions shown on the surfaces in Fig. 20(a). For a fixed value of the load parameter, the optimum value of the energy dissipation parameter is achieved by increasing porosity, decreasing aggregate, and increasing fibers in the proportions shown on the surfaces in Fig. 20(b).

With the independent variables specified, the ranges of the output variables or the performance parameters can be determined. This is shown in Fig. 21, which quantifies the ranges of η_1, η_2, and η_3 for the microstructural settings considered in this study (design space in Fig. 1). Values of the two performance parameters lying off the surface are not attainable for any microstructural composition within the design space ($10\% \le V_f^a \le 40\%$, $0\% \le V_f^f \le 10\%$, and $0\% \le V_f^p \le 5\%$). The shading of the surface in the figure corresponds to the value of the combined performance parameter η_1. Because the combined performance parameter η_1 is the product of η_2 and η_3, η_1 is clearly larger when the two individual parameters are larger. However, the figure
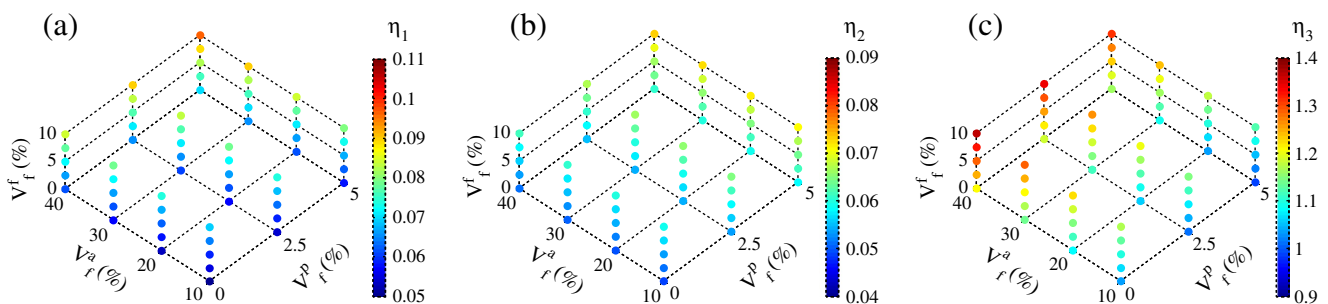

Fig. 19. Values of the microstructure performance parameters for the microstructure designs analyzed: (a) η_1, (b) η_2, (c) η_3.
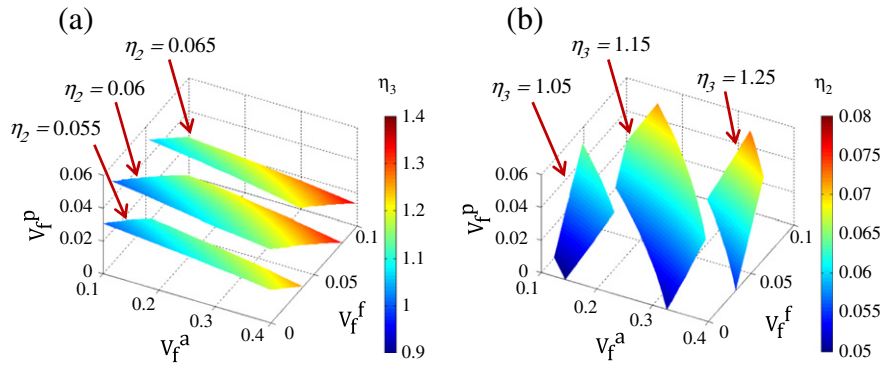
Fig. 20. Isosurfaces within the design space of Fig. 1 showing (a) surfaces with constant values of η_2 and (b) surfaces with constant values of η_3.

shows that it is impossible to maximize both η_2 and η_3 within the bounds of the design space considered in this study and higher values for them are possible for design settings outside the space considered.

6. Conclusions

A material must balance strength with the ability to dissipate energy to be most effective in blast- and impact-resistant protective structures. Ultra-high performance concrete is a building material that provides the benefits of traditional concrete along with increased strength and durability. However, due to its novelty and wide range of possible microstructures, the relationship between the dynamic behavior of UHPC and its microstructures is not well quantified. In an effort to provide useful information for materials design, the load-carrying and energy-dissipation capabilities of UHPC under dynamic loading are evaluated over a parametric range of volume fractions of constituent phases. To this end, a series of numerical simulations are carried out, explicitly accounting for the distributions of quartz aggregate, steel fibers, and porosity.

The conclusions of this study relating to the load-carrying and energy-dissipation capacities are:

(1) The volume fractions of constituent phases have a significantly larger influence on the energy-dissipation capacity than on the load-carrying capacity of UHPC. The load-carrying capacity is

Fig. 21. Ranges of η_1, η_2, and η_3 for the microstructural settings considered in this study (design space in Fig. 1).

largely related to density, which affects the longitudinal elastic wave speed and the elastic stiffness of the material. These quantities in turn determine the reaction stress carried by the material.

(2) The propagating stress wave does not show appreciable attenuation in magnitude for the size and time scales considered in this study. This is likely due to the fact that all microstructures dissipate less than 10% of the externally applied work. Active dissipation occurs primarily at the wave front, partly due to the high level of confinement or stress triaxiality of the nominally uniaxial strain deformation condition. Behind the stress wave, the rate of energy dissipation is on the order of 10^3 times smaller than the rate on the cusp of the wave front. Furthermore, the magnitude of dissipation shows little attenuation throughout the length of a UHPC microstructure for the microstructural settings considered.

(3) Fibers and porosity have competing effects on energy dissipation through interface fracture and friction, while aggregate and porosity have a synergistic effect on the energy dissipated through interface fracture. Furthermore, porosity alters the role played by fibers in the frictional dissipation process. At low-porosity and aggregate levels, increasing the fiber volume fraction can increase frictional dissipation between the fibers and cementitious matrix by over 12%. At high-porosity and aggregate levels, increasing the fiber volume fraction arrests crack propagation facilitated by the presence of porosity and can decrease frictional dissipation by over 17%. At low-aggregate levels, increasing the porosity can increase frictional dissipation by nearly 30%. At higher aggregate levels, increasing the porosity can increase frictional dissipation by nearly 40%.

(4) The crack density within UHPC is approximately proportional to the energy dissipated through damage and fracture. The constant of proportionality can provide an average interface fracture energy of the constituents of UHPC.

(5) Inelastic deformation (granular flow of the matrix and plastic deformation of the fibers) contributes approximately 70% to 85% of the total energy dissipation, interfacial frictional dissipation contributes approximately 15% to 30%, and damage accounts for less than 0.5%. Efforts to increase the energy absorbency of UHPC should focus on enhancing inelastic deformation and internal friction, as improvements to these two energy dissipation components have much larger effects than improvements to the interface fracture energy.

(6) Microstructure–performance relations have been developed that can be used in the design of UHPC structures that must be tailored to mitigate specific loads. The bounds on these parameters are determined by the microstructural settings considered in this study. Results show that microstructures with very different compositions can have similar dynamic behaviors under compressive loads.
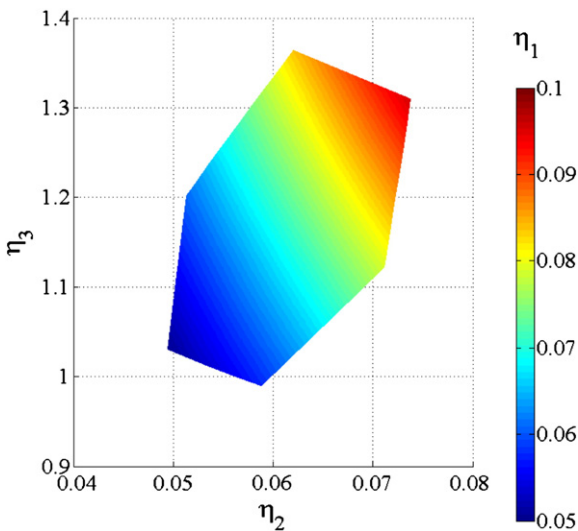
Finally, it is instructive to note that the relations and results described in this paper are applicable for the design space, material setting and loading conditions considered. Factors not considered include, e.g., the variation of pore size and fiber diameters. These factors are additional dimensions in the microstructure design space and should be considered in future studies. It is important to note that higher temperatures can result from high strain-rate dynamic loading, leading to thermally driven events in materials. The analysis reported here does not account for processes such as temperature-induced phase transformation in the quartz aggregate and thermal softening of the steel fibers or cementitious matrix. The high pressures resulting from the dynamic loading can also induce phase transformations in the constituents. The α-quartz-to-coesite phase transformation is one such example. The effect of this phase transformation is analyzed in [21] as a companion study reported in this paper. Finally, it should be pointed out that, although the study here concerns only one form of UHPC, the framework developed is applicable to other heterogeneous materials. For example, there has been increasing interest in using polymeric fibers (e.g. PVA and polypropylene) or carbon nanofibers instead of steel fibers in UHPC. Similar studies can be carried out for such material systems using this framework.

Acknowledgments

References

[1] Z. Rong, W. Sun, Y. Zhang, Dynamic compression behavior of ultra-high performance cement based composites, Int. J. Impact Eng. 37 (2010) 515–520.
[2] W. Sun, J. Lai, Dynamic mechanical behavior and durability of ultra high-performance cementitious composite, Key Eng. Mater. 400 (2009) 3–15.
[3] G.K. Schleyer, S.J. Barnett, S.G. Millar, G. Wight, Modeling the Response of UHPFRC Panels to Explosive Loading, in: International Conference on Structures under Shock and Impact, WIT Press, Tallinn, Estonia, 2010, pp. 173–184.
[4] M. Rebentrost, G. Wight, Behavior and resistance of ultra high-performance concrete to blast effects, in: S. Sturwald (Ed.), Second International Symposium on Ultra High-Performance Concrete, Kassel University Press, Kassel, Germany, 2008, pp. 735–742.
[5] B. Cavil, M. Rebentrost, V. Perry, Ductal — An Ultra-High Performance Material for Resistance to Blast and Impacts, in: 1st Specialty Conference on Disaster Mitigation, Calgary, Alberta, Canada, 2006.
[6] Z. Mroz, M. Angelillo, Rate-Dependent Degradation Model for Concrete and Rock, in: International Symposium on Numerical Models in Geomechanics, Zurich, 1982, pp. 208–217.
[7] G.Z. Voyiadjis, Z.N. Taqieddin, Elastic plastic and damage model for concrete materials: Part I — Theoretical formulation, Int. J. Struct. Changes Solids 1 (2009) 31–59.
[8] D. Fanella, D. Krajcinovic, A micromechanical model for concrete in compression, Eng. Fract. Mech. 29 (1988) 49–66.
[9] P. Grassl, M. Jirásek, Damage-plastic model for concrete failure, Int. J. Solids Struct. 43 (2006) 7166–7196.
[10] Z. Tu, Y. Lu, Evaluation of typical concrete material models used in hydrocodes for high dynamic response simulations, Int. J. Impact Eng. 36 (2009) 132–146.
[11] S.W. Park, Q. Xia, M. Zhou, Dynamic behavior of concrete at high strain rates and pressures: II. Numerical simulation, Int. J. Impact Eng. 25 (2001) 887–910.
[12] F.T.S. Aragao, Y.-R. Kim, J. Lee, D.H. Allen, Micromechanical model for heterogeneous asphalt concrete mixtures subjected to fracture failure, J. Mater. Civ. Eng. 23 (2011) 30–38.
[13] Z. Xu, H. Hao, H.N. Li, Mesoscale modelling of fibre reinforced concrete material under compressive impact loading, Constr. Build. Mater. 26 (2012) 274–288.
[14] J.E. Bolander, Y.M. Lim, Simulations of Fiber Distribution Effects in Fiber-Reinforced Cement Composites, in: AIP Conference Proceedings, 973, 2008, pp. 507–512.
[15] C. Lammi, D. McDowell, M. Zhou, Computation of the Mesoscale Dynamic Fracture and Dissipation Behavior of Concrete, Comput. Mech. (submitted for publication).
[16] B. Ellis, D. McDowell, M. Zhou, Energy Dissipation and Evolving Strength of Ultra-High-Performance Fiber-Reinforced Concrete (UHPFRC), in: 3rd International Symposium on Ultra-High Performance Concrete and Nanotechnology for High Performance Construction Materials, Kassel, Germany, submitted for publication.
[17] E.N. Landis, J.E. Bolander, Explicit representation of physical processes in concrete fracture, J. Phys. D: Appl. Phys. 42 (2009) 214002.
[18] Y. Farnam, S. Mohammadi, M. Shekarchi, Experimental and numerical investigations of low velocity impact behavior of high-performance fiber-reinforced cement based composite, Int. J. Impact Eng. 37 (2010) 220–229.
[19] F. Bencardino, L. Rizzuti, G. Spadea, R. Swamy, Stress–strain behavior of steel fiber-reinforced concrete in compression, J. Mater. Civ. Eng. 20 (2008) 255–263.
[20] H.W. Reinhardt, P. Rossi, R. Baggott, G. Balazs, J.E. Bolander, A.E. Brandt, M. Cheyrezy, K. Chong, L. Eredelyi, H. Krenchel, D. Lange, C. Leung, V.C. Li, H. Mihashi, A.E. Naaman, V.S. Parameswaran, H. Stang, Future research needs in the field of HPFRCC, in: A.E. Naaman, H.W. Reinhardt (Eds.), High Performance Fiber Reinforced Cement Composites, 2, E&FN Spon, Ann Arbor, USA, 1995, p. 463.
[21] J.J. Buck, D.L. McDowell, M. Zhou, Effect of α-quartz-to-coesite silica phase transformation on the dynamic behavior of UHPC, submitted for, publication.
[22] ABAQUS Theory Manual, Simulia, 2010.
[23] D.C. Drucker, W. Prager, Soil mechanics and plastic analysis or limit design, Q. Appl. Math. 10 (1952) 157–165.
[24] X.Q. Zhou, V.A. Kuznetsov, H. Hao, J. Waschl, Numerical prediction of concrete slab response to blast loading, Int. J. Impact Eng. 35 (2008) 1186–1200.
[25] V. Li, Determination of interfacial debond mode for fiber-reinforced cementitious composites, J. Eng. Mech. 120 (1994) 707–720.
[26] B. Shen, G.H. Paulino, Identification of cohesive zone model and elastic parameters of fiber-reinforced cementitious composites using digital image correlation and a hybrid inverse technique, Cem. Concr. Compos. 33 (2011) 572–585.
[27] A. Hillerborg, M. Modeer, P.E. Petersson, Analysis of crack formation and crack growth in concrete by means of fracture mechanics and finite elements, Cem. Concrete Res. 6 (1976) 773–782.
[28] A. Gens, I. Carol, E.E. Alonso, An interface element formulation for the analysis of soil-reinforcement interaction, Comput. Geotech. 7 (1989) 133–151.
[29] P.P. Camanho, C.G. Davila, M.F. de Moura, Numerical simulation of mixed-mode progressive delamination in composite materials, J. Compos. Mater. 37 (2003) 1415–1438.
[30] P.E. Petersson, Crack growth and development of fracture zone in plane concrete and similar materials, Lund Institute of Technology, Lund, Sweden, 1981.
[31] J. Roesler, G.H. Paulino, K. Park, C. Gaedicke, Concrete fracture prediction using bi-linear softening, Cem. Concr. Compos. 29 (2007) 300–312.
[32] M.L. Benzeggagh, M. Kenane, Measurement of mixed-mode delamination fracture toughness of unidirectional glass/epoxy composites with mixed-mode bending apparatus, Compos. Sci. Technol. 56 (1996) 439–449.
[33] A.B. Abell, D.A. Lange, Fracture mechanics modeling using images of fractured surfaces, Int. J. Solids Struct. 35 (1998) 4025–4033.
[34] G.T. Camacho, M. Ortiz, Computational modelling of impact damage in brittle materials, Int. J. Solids Struct. 33 (1996) 2899–2938.
[35] In: Building Code Requirements for Structural Concrete (ACI 318–95), American Concrete Institute, Farmington Hills, Michigan, 1995, p. 369.
[36] I. Carol, C.M. López, O. Roa, Micromechanical analysis of quasi-brittle materials using fracture-based interface elements, Int. J. Numer. Methods Eng. 52 (2001) 193–215.
[37] C.M. Sayers, M. Kachanov, A simple technique for finding effective elastic constants of cracked solids for arbitrary crack orientation statistics, Int. J. Solids Struct. 27 (1991) 671–680.
[38] F. Homand, D. Hoxha, T. Belem, M.-N. Pons, N. Hoteit, Geometric analysis of damaged microcracking in granites, Mech. Mater. 32 (2000) 361–376.